A regularized approach for processing full-polarimetric data in synthetic aperture imaging radiometry

E. Anterrieu [a] and P. Waldteufel [b]

[a] OMP-UMR5572, 14 avenue Edouard Belin, 31400 Toulouse, FRANCE – Eric.Anterrieu@ast.obs-mip.fr
[b] IPSL/SA-UMR7620, B.P. 3, 91371 Verrières le Buisson, FRANCE – Philippe.Waldteufel@aerov.jussieu.fr

Abstract – Synthetic Aperture Imaging Radiometers (SAIR) are powerful sensors for high-resolution observations of the Earth at low microwaves frequencies. This contribution extends the concept of "band-limited resolving matrix" for retrieving brightness temperature maps from complex visibilities measurements to the case of the processing of full-polarimetric data.

Keywords: SMOS, aperture synthesis, imaging radiometry, full polarization, inverse problem.

1. INTRODUCTION

The SMOS (Soil Moisture and Ocean Salinity) space mission is an ESA (European Space Agency) led project aimed at global monitoring of surface soil moisture and sea surface salinity from L-band space borne observations (Kerr, 2001). It will be the first attempt to apply to remote sensing of the Earth surface, the concept of imaging interferometric radiometry by aperture synthesis, initially developed for radio astronomy.
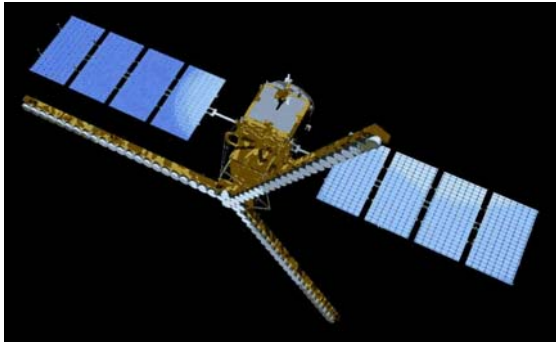

Figure 1. Artist view of the SMOS project.

Interferometer measurements, also called complex visibilities, are obtained by cross-correlating the signals collected by pairs of spatially separated antennae which have overlapping fields of view. Visibility samples are related to the radiometric brightness temperature of the observed scene by a spatial Fourier-like integral. However, due to the angular extent of the target, the conditions, which typically apply for radio astronomy observations, are no longer valid for Earth remote sensing. As a consequence, the standard imaging algorithms developed by radio astronomers are not convenient for retrieving brightness temperatures of the scene from complex visibilities. Moreover, the corresponding inverse problem is often ill-posed unless a regularizing constraint is introduced in order to provide a unique and stable solution to the problem (Lannes, 2001). The finite physical size of a synthetic antenna results in a truncation of the visibility samples above a certain spatial frequency. As we can see in Fig. 1, the Y-shaped array selected for SMOS is fitted with 72

equally spaced elements. This kind of array leads to complex visibilities sampled over a hexagonal grid inside a star-shaped window in the Fourier domain. This band-limited property is taken into account for regularizing the inverse problem (Lannes, 1996) and the relationship between complex visibilities and brightness temperatures is rephrased in the Fourier domain: the unknowns are the Fourier components of the scene brightness temperature. Thanks to spatial redundancies, the number of these Fourier components inside the star-shaped window is smaller than the number of visibility samples: the over-determined regularized inverse problem is solved in the least-squares sense. This contribution extends the concept of the "resolving matrix" (Anterrieu, 2004) to the case of the processing of full-polarimetric data. To support the theory and to illustrate the performances of this imaging method, numerical simulations are presented within the frame of the SMOS project.

2. THEORETICAL FRAMEWORK

SAIRs devoted to Earth observation measure the correlation between the signals collected by pairs of spatially separated antennas A_k and A_l which have overlapping fields of view, yielding samples of the visibility function V, also termed complex visibilities, of the brightness temperature map T of the observed scene.

2.1. Direct problem

The relationship between T and V is given by the spatial Fourier-like integral (Ruf, 1988):

$$V(u_{kl}) \propto \iint_{\|\xi\|^2 \leq 1} \frac{F_k(\xi)\, F_l(\xi)}{\sqrt{1-\xi^2}} T(\xi)\, \tilde{r}(\frac{-u_{kl}\xi}{f_o})\, e^{-2j\pi u_{kl}\xi}\, d\xi \qquad (1)$$

The components $\xi_1 = \sin\theta\cos\phi$ and $\xi_2 = \sin\theta\sin\phi$ of the angular position variable $\xi = (\xi_1,\xi_2)$ are direction cosines (θ and ϕ are the traditional spherical coordinates), u_{kl} is the spatial frequency associated with the two antennas A_k and A_l (namely, the spacing between the antennas normalized to the central wavelength of observation $\lambda_o = c/f_o$), F_k and F_l are the voltage patterns of the antennas, $\tilde{r}$ is the fringe-wash function which accounts for decorrelation effects, $t = u_{kl}\xi/f_o$ is the spatial delay and $f_o = 1.415$ GHz is the central frequency of observation.

Denoting by L the number of antennas of the interferometric array, the number of complex visibilities provided by the interferometer is equal to L(L-1)/2 when accounting for the hermitian property of (1). However, the list of spatial frequencies u_{kl} is not necessarily non redundant since two different pairs of antennas may lead to the same spatial frequency.

Since SAIR have limited dimensions, the spatial frequencies u_{kl} sampled by an interferometer are confined to a limited region of the Fourier domain, the so-called experimental frequency coverage H. Moreover, in the case of SMOS the visibility samples

are obtained from raw data inside a star-shaped window H over an hexagonally sampled grid G_u in the Fourier domain.

For computational purposes, numerical quadrature is used to represent integral (1) as a summation over N^2 integrand samples, the N^2 pixels of the spatial grid G_ξ which is the dual grid of G_u. The number of pixels in the grids G_u and G_ξ is chosen in such a way that the Shannon criterion is satisfied and the numerical quadrature is sufficiently accurate (Anterrieu, 2004).

2.2. Inverse problem

The inverse problem aims at inverting the discrete version of relation (1) to retrieve T from V, i.e. solving the linear system:

$$\mathbf{G}T = V \tag{2}$$

where $\mathbf{G}$ is the discrete linear modeling operator from the object space E into the data space F describing the basic relation (1).

Since the direct problem is stated *via* an integral equation, the inverse problem does not usually have a straightforward solution. Moreover, since the dimension of the object space E (here the N^2 pixels used to sample T) is often larger than the dimension of the data space F (the $L(L-1)/2$ samples of V), the linear system (2) is an under-constrained problem with multiple solutions for T. Consequently, the minimum of the least-square criterion

$$\min_{T \in E} \|V - \mathbf{G}T\|_F^2 \tag{3}$$

which is also the solution of the normal equation $\mathbf{G}^*\mathbf{G}\,T = \mathbf{G}^*\,V$, is therefore not unique because the square matrix $\mathbf{G}^*\mathbf{G}$ is singular. Thus, according to the definition given by Hadamard (Bertero, 1998), the inverse problem is ill-posed and has to be regularized in order to provide a unique and stable solution for T.

2.3. Band-limited regularization

Referring to a physical concept, namely the limited resolution of SAIR, a recently proposed approach (Anterrieu, 2004) is to find the temperature map T_r which has its Fourier transform confined to the experimental frequency coverage H. This band-limited solution realizes the minimum of the constrained problem

$$\begin{cases} \min_{T \in E} \|V - \mathbf{G}T\|_F^2 \\ (\mathbf{I} - \mathbf{P_H})T = 0 \end{cases} \tag{4}$$

where $\mathbf{P_H}$ is the projector onto the subspace E_H (of E) of the H-band limited functions. The unique solution of (4) is given by:

$$T_r = \mathbf{U}^* \mathbf{Z} \mathbf{A}^+ V \tag{5}$$

where $\mathbf{A}^+ = (\mathbf{A}^*\mathbf{A})^{-1}\mathbf{A}^*$ is the More-Penrose pseudo-inverse of the rectangular matrix $\mathbf{A} = \mathbf{G}\,\mathbf{U}^*\,\mathbf{Z}$, $\mathbf{U}$ is the Fourier transform operator and $\mathbf{Z}$ is the zero-padding operator beyond H.

2.4. Extension to the four Stokes parameters

When taking into account the full-polarimetric mode of the instrument, relation (1) becomes (Waldteufel, 2002):

$$\begin{bmatrix} V_1(u_{kl}) \\ V_2(u_{kl}) \\ V_3(u_{kl}) \\ V_4(u_{kl}) \end{bmatrix} \propto \iint_{\|\xi\|^2 \leq 1} \frac{\mathbf{F}_{kl}(\xi)}{\sqrt{1-\xi^2}} \begin{bmatrix} T_1(\xi) \\ T_2(\xi) \\ T_3(\xi) \\ T_4(\xi) \end{bmatrix} \tilde{r}(\frac{-u_{kl}\xi}{f_o}) e^{-2j\pi u_{kl}\xi} d\xi \tag{6}$$

where $\mathbf{F}_{kl}$ is a 4×4 matrix involving the co-polar and cross-polar voltage patterns on ports X and Y of the antennas A_k and A_l. Shown in Fig. 2 are examples of such co-polar and cross-polar voltage patterns for an airborne demonstrator with 10 antennas.
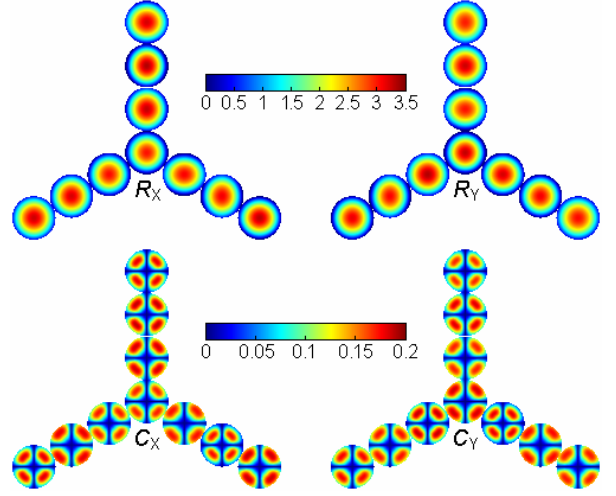

Figure 2. Amplitude of co-polar (*top*, R_x and R_y) and cross-polar (*bottom*, C_x and C_y) antenna gains. The maximum value of the cross-polar gains is here 25 dB below that of the co-polar ones.

Consequently, the new modeling matrix $\mathbf{G}$ is $4 \times 4 = 16$ times larger than the previous one. Indeed, the dimension of the new data space F is 4 times larger than the previous one because now the data are $V = [V_1, V_2, V_3, V_4]$. Likewise, the dimension of the new object space E is 4 times larger than the previous one because now the unknown maps are $T = [T_1, T_2, T_3, T_4]$. As we can see in Fig. 3, depending on the level of the coupling between the co-polar and cross-polar voltage patterns, this new $\mathbf{G}$ matrix can exhibit a block-diagonal structure, or not.
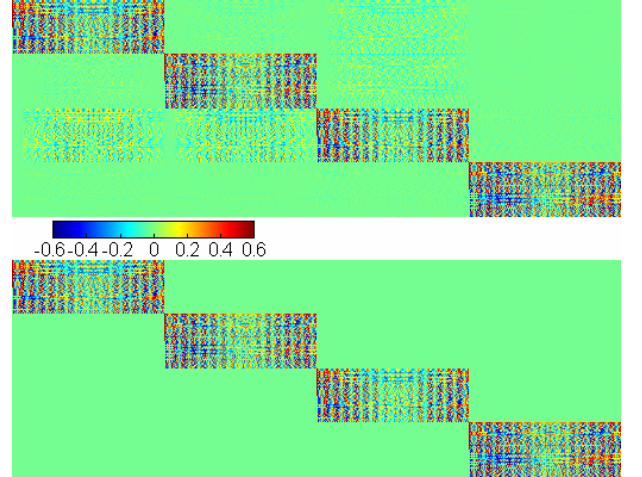

Figure 3. Two modeling matrices $\mathbf{G}$ with coupling level 25 dB (*bottom*) or only 10 dB (*top*).

3. NUMERICAL SIMULATIONS

Simulations have been performed for a Y-shaped array equipped with $L = 10$ antennas. The number of complex visibilities is

therefore equal to L(L-1)/2 = 45, that is to say 90+1=91 real numbers per Stokes parameter when adding one measurement for the zero spacing in the modeling of the instrument. The dimension of the hexagonally sampled grids G_u and G_ξ has been fixed to N^2=256 for each Stokes parameter. The size of the real-valued matrix **G** is therefore 364×1024. Simulations have been performed for the two modeling matrices **G** shown in Fig. 3. In both case, the reconstruction have been performed with the full modeling matrix and with only the four diagonal blocks

The brightness temperature maps $T = [T_1, T_2, T_3, T_4]$ used for these simulations are shown in Fig. 4 at their highest level of resolution and in Fig. 5 at the resolution level of the instrument and damped with a Hanning window (Anterrieu, 2002) $T_w = T * W$.
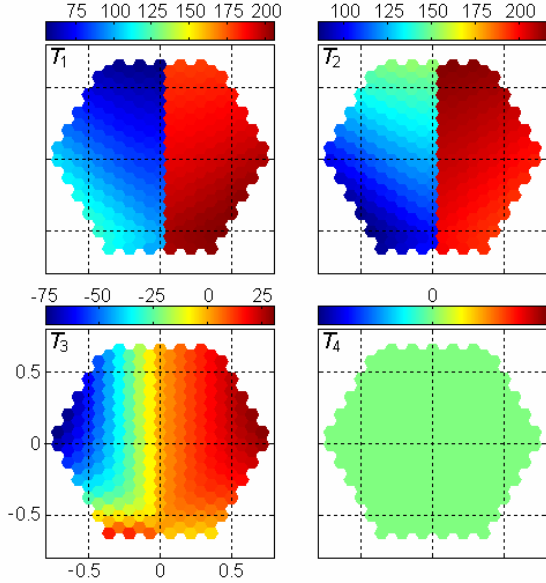
Complex visibilities $V = [V_1, V_2, V_3, V_4]$ have been first simulated from the high-resolution maps $T = [T_1, T_2, T_3, T_4]$ shown in Fig. 4 for a modeling matrix **G** with a coupling level equal to 25 dB. The reconstructed brightness temperature maps $T_r = [T_{r1}, T_{r2}, T_{r3}, T_{r4}]$ obtained with the full modeling **G** matrix are shown in Fig. 6 at the resolution level of the instrument and damped with the Hanning window W. These maps should be compared to those in Fig. 5. The corresponding error maps $\Delta T = T_r - T_w$, are shown in Fig. 7 and the rms errors are respectively equal to 0.55 K, 0.50 K, 0.30 K and 0.04 K. When the reconstruction is performed with only the four diagonal blocks of the modeling **G** matrix, i.e. when coupling is ignored, these numbers become 0.99 K, 1.25 K, 2.92 K and 0.86 K, respectively.

Figure 4. Brightness temperature maps of the four Stokes parameters at their highest level of resolution.

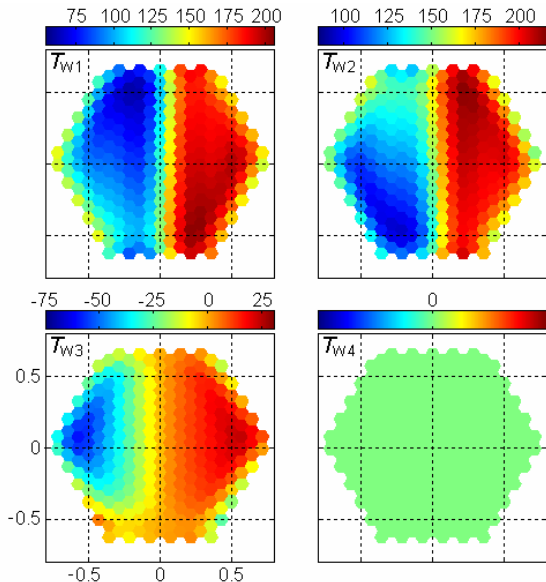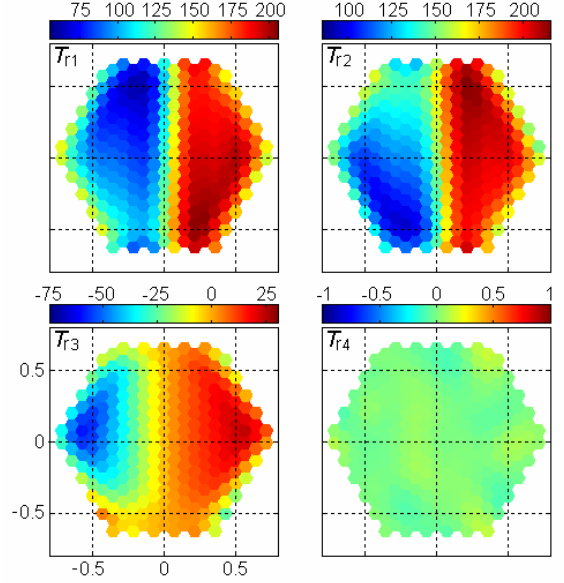Figure 6. Reconstructed maps when the full modeling **G** matrix is taken into account with a coupling level equal to 25 dB.

Figure 5. Brightness temperature maps of the four Stokes parameters at the level of resolution of the instrument.
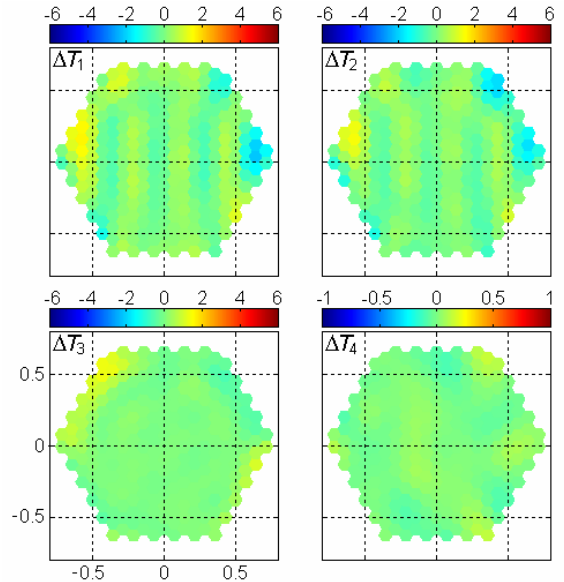

Figure 7. Error maps of the reconstructed maps shown in Fig. 6.

Complex visibilities V have been next simulated from the same high-resolution maps T shown in Fig. 4 but now for a modeling matrix $\mathbf{G}$ with a coupling level equal to 10 dB. The reconstructed brightness temperature maps T_r obtained with the full modeling $\mathbf{G}$ matrix are shown in Fig. 8 at the resolution level of the instrument and damped with the Hanning window W. These maps should be compared to those in Fig. 5. The corresponding error maps $\Delta T = T_r - T_w$, are shown in Fig. 9 and the rms errors are respectively equal to 0.95 K, 0.50 K, 0.64 K and 0.10 K. When the reconstruction is performed with only the four diagonal blocks of the modeling $\mathbf{G}$ matrix, i.e. when coupling is ignored, these numbers become 13.2 K, 11.9 K, 20.3 K and 2.6 K, respectively.
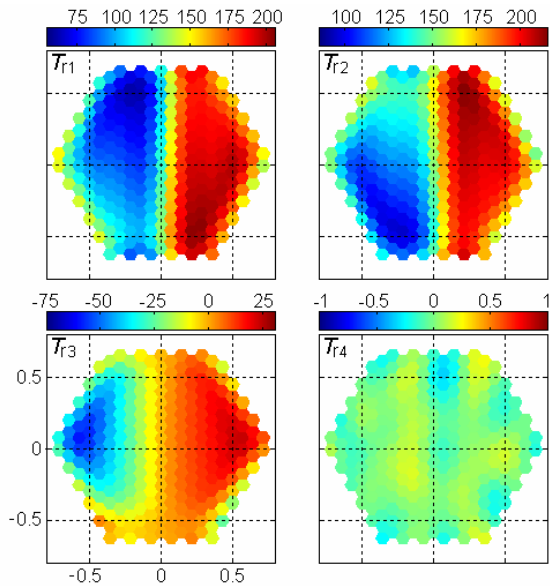

Figure8. Reconstructed maps when the full modeling $\mathbf{G}$ matrix is taken into account with a coupling level equal to 10 dB.
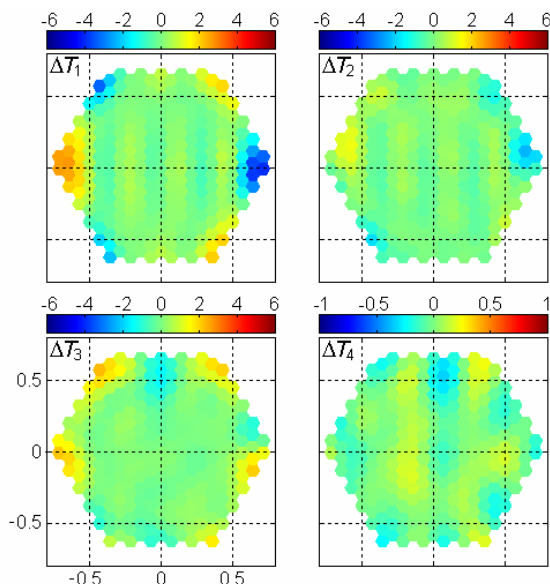

Figure 9. Error maps of the reconstructed maps shown in Fig. 8.

4. CONCLUSION

This contribution has extended the concept of the "resolving matrix" to the case of the processing of full-polarimetric data within the frame of the SMOS project. It has been shown that the reconstruction process cannot be reduced to four independent ones (of smaller size) for every Stokes parameters, even when the co-polar and cross-polar coupling is very low. The overall robustness of the "resolving matrix" approach is preserved when retrieving the four Stokes components of the brightness temperature by solving a linear system which is 16 times larger than the standard one. Thus, the regularization principle does not suffer from any size effect and, to a certain extent, from the coupling level. Of course, these first concluding comments have to be confirmed with simulations conducted for the spatial instrument with 72 antennas (the size of the real-valued full-polarization modeling matrix $\mathbf{G}$ is therefore 20452×65536).

5. ACKNOWLEDGEMENTS

6. REFERENCES

E. Anterrieu, "A resolving matrix approach for synthetic aperture imaging radiometers", IEEE Trans. on Geosc. and Remote Sens., 42(**8**), pp. 1649-1656, 2004.

E. Anterrieu, P. Waldteufel, and A. Lannes, "Apodization functions for 2D hexagonally sampled synthetic aperture imaging radiometers", IEEE Trans. on Geosc. and Remote Sens., 40(**12**), pp. 2531-2542, 2002.

M. Bertero and P. Boccacci, "Introduction to Inverse Problems in Imaging", Institute of Physics Publishing, 1998.

Y.H. Kerr, P. Waldteufel, J.-P. Wigneron, J.-M. Martinuzzi, J. Font, and M. Berger, „Soil Moisture Retrieval from Space: The Soil Moisture and Ocean Salinity (SMOS) Mission", IEEE Trans. on Geosc. and Remote Sens., 39(**8**), pp. 1729-1735, 2001.

A. Lannes, E. Anterrieu, and K. Bouyoucef, "Fourier Interpolation and Reconstruction via Shannon-type Techniques; Part I: regularization principle", J. of Mod. Optics, 41(**8**), pp. 1537-1574, 1994.

A. Lannes, E. Anterrieu, and K. Bouyoucef, "Fourier Interpolation and Reconstruction via Shannon-type Techniques; Part II: technical developments and applications", J. of Mod. Optics, 43(**1**), pp. 105-138, 1996.

C.S. Ruf, C.T. Swift, A.B. Tanner, and D.M. LeVine, "Interferometric synthetic aperture radiometry for the remote sensing of the Earth", IEEE Trans. on Geosc. and Remote Sens., 26(**5**), pp. 597-611, 1988.

P. Waldteufel and G. Caudal, "About off-axis radiometric polarimetric measurements", IEEE Trans. on Geosc. and Remote Sens., 40(**6**), pp. 1435-1439, 2002.